Pure Appl. Geophys.

DOI 10.1007/s00024-012-0463-y

Pure and Applied Geophysics

Shear Band Formation in Numerical Simulations Applying a Continuum Damage Rheology Model

Yaron Finzi,[1] Hans Muhlhaus,[1] Lutz Gross,[1] and Artak Amirbekyan[1]

Abstract—In seismically active regions, faults nucleate, propagate, and form networks that evolve over time. To simulate crustal faulting processes, including the evolution of fault-zone properties, a rheological model must incorporate concepts such as damage rheology that describe the various stages of the seismic cycle (strain localization, subcritical crack growth and macroscopic failure) while accounting for material degradation and healing and off-fault deformation. Here we study the fundamental patterns of strain-localisation within the framework of a continuum damage rheology by performing a shear band analysis (linear instability analysis) and comparing predictions of shear band orientations with numerical results of the nonlinear problem. We find (analytically and numerically) that the angle between the shear band and the less compressive (transverse) direction is between 47° in compression tests with a strain ratio of 0.25 (highly confined compression test), and 60° for a strain ratio higher than 1.4 (axial compression and transverse extension). In addition we find that shear bands exhibit local dilation ($I_1 > 0$) in a wide range of strain ratios excluding only simulations with highly confined compression (which yield compacting shear bands or non-localized deformation). Finally, we discuss the applicability of the damage model for simulating deformation in the seismogenic, brittle crust.

1. Introduction

The brittle crust consists of structural and material heterogeneities of every scale making it highly susceptible to strain localization in the form of fault nucleation, propagation and the formation of fault networks. Progressive strain localisation and periodic fault system re-configuration alter the geometrical complexity and internal structure of fault systems. Fault structure and fault system complexity have a major effect on seismicity patterns, earthquake-related ground shaking, fluid flow and mineralisation. However, most studies of fault systems represent fault zones as pre-defined, fixed planar features, ignoring processes of fault nucleation and propagation, and ignoring the evolution of fault-zone rheology.

To better simulate long-term crustal deformation including fault nucleation and propagation (i.e., creation of new frictional surfaces) a numerical model should incorporate concepts of fracture mechanics and material degradation. Continuum damage rheology models (e.g., Malvern, 1969; Budiansky and O'Connell 1976; Allix and Hild, 2002) are particularly suitable for lithospheric deformation studies as they describe the brittle portion of the Earth's lithosphere as "damaged" in the sense that it contains an evolving distribution of weakened material (Lyakhovsky and Myasnikov, 1984; Turcotte and Glasscoe, 2004). This view is supported by studies of fault-zone structures (e.g., Chester *et al.*, 1993; Evans *et al.*, 2000; Sibson, 2003; Ben-Zion and Sammis, 2003; Kim *et al.*, 2004), and laboratory studies of brittle deformation (e.g., Alm *et al.*, 1985; Lockner *et al.*, 1992; Hamiel *et al.*, 2004a). In such rheology models, a damage state variable modifies the elastic properties of lithospheric materials, enabling the simulation of fault nucleation and evolution, including both damage accumulation and healing of fault-zone materials.

The current work complements ongoing efforts to build a numerical model suitable for the study of the long term structural evolution of regional fault systems. For this we study strain localization within the framework of an established damage rheology model (Lyakhovsky *et al.*, 1997a, b, 2001), and we incorporate this model in the finite element based partial differential equations (PDEs) solver Escript (Gross *et al.*, 2007; also see https://launchpad.net/escript-finley/). The formulation of the applied rheology

[1] Earth Systems Science Computational Centre, School of Earth Science, The University of Queensland, St. Lucia, QLD 4072, Australia. E-mail: y.finzi@uq.edu.au

Published online: 03 April 2012

model and its implementation in Escript are described in Sect. 2, followed by a linear-instability analysis which illuminates the conditions for shear band formation (Sect. 3). The fundamental aspects of strain localization and shear band formation in this damage rheology framework are the focus of this publication.

On a global scale, the rheology needed to describe deformation in the lithosphere is highly non-linear, and near the surface, where temperatures are less than approximately 600 °C, it becomes necessary to consider the role of plasticity (Hill, 1998; Lubliner, 1990) and elasticity (Watts *et al.*, 1980). Continental-scale structures experiencing large elastic–plastic deformations typically undergo a succession of instabilities. For instance, a plate in extension will deform initially in a uniform fashion until, at a critical stress level, a neck forms around the symmetry axis of the deformation (Biot, 1965; Buck 1991; England, 1983; Gibbs, 1984; Hill and Hutchinson, 1975; Moresi and Muhlhaus, 2006; Tvergaard *et al.*, 1981; Walsh *et al.*, 1991). Subsequently, shear bands form within the region of the neck. Once the shear bands are established the deformation of the plate is carried almost exclusively by the deformations of the bands, more or less passively accommodated by the elastic deformations of the surrounding material.

Shear-bands have long been recognized as a most significant mechanism of strain-localization and macroscopic failure in brittle and plastic deformation processes of a very wide range of scales (e.g., Rudnicki and Rice, 1975; Muhlhaus and Vardoulakis, 1987; Hobbs *et al.*, 1990; Moresi and Muhlhaus, 2006; Lemiale *et al.*, 2008). In the crust, shear bands or faults are arguably the most important deformation mechanism. They occur on many different scales, e.g., in the form of detachment faults in rift zones or as collapse mechanisms of geotechnical structures (e.g., Chen, 1975). Various field studies yielded high resolution descriptions of crustal deformation structures confirming that strain along active and exhumed faults is highly localized within a narrow (10–20 cm) "fault-core" surrounded by a damage-zone (e.g., Rice, 1983; Chester and Logan, 1986; Schulz and Evans, 2000; Rockwell and Ben-Zion, 2007). The damage-zone is typically defined as the region in which the density of deformation features exceeds the average regional level in the surrounding host rock (Chester *et al.*, 1993; Ben-Zion and Sammis, 2003; Mitchell and Faulkner, 2009). Regardless of the deformation length scale, the stress and temperature conditions under which shear bands form depend strongly on the local material behavior and as such on the details of the constitutive relationships.

In Sect. 3 we perform a shear band analysis of our damage rheology and compare theoretical properties of the shear-bands with numerical results. In Sect. 4.1 we describe the volumetric strain patterns in our simulated shear-bands and discuss our observations in light of the growing volume of studies on the topic of compaction bands (e.g., Aydin *et al.*, 2006; Holocomb *et al.* 2007; Schultz *et al.*, 2008). Finally, In Sect. 4.2 we discuss the applicability of the damage rheology model for simulations of crustal deformation.

2. *Theory and Numerical Formulation*

2.1. *Theoretical Background*

We base our investigation on a thermodynamically-based continuum damage model proposed by (Lyakhovsky *et al.*, 1997a, b; Hamiel *et al.*, 2004a). This damage rheology is applicable to volumes with a sufficiently large number of cracks that allow quantitative description through properties of the crack distribution rather than those of the individual cracks (Lyakhovsky and Myasnikov, 1984, 1985). Detailed reviews and recent developments of the model can be found in Ben-Zion and Lyakhovsky (2006) and Lyakhovsky and Ben-Zion (2008), examples of model applications showing the dominant role damage processes play in the evolution of fault systems and their internal structure can be found in Finzi *et al.* (2009, 2011) and Ben-Zion (2008). Here we only summarize the main ingredients of the model that are relevant for our work.

The effects of distributed cracks (i.e., existing damage) on the elastic properties of a solid are accounted for in the damage model by generalizing the strain energy function:

$$U = \frac{1}{\rho}\left(\frac{\lambda}{2}I_1^2 + \mu I_2 - \gamma I_1\sqrt{I_2}\right) \qquad (1)$$

where $I_1 = \varepsilon_{kk}$ and $I_2 = \varepsilon_{ij}\varepsilon_{ij}$ are the first and second invariants of the elastic strain tensor ε^{e}_{ij}, ρ is the mass

density, λ and μ are the Lamé parameters, and γ is a third modulus of a damaged solid. The first two terms of Eq. (1) give the classical strain potential of linear elasticity (e.g., MALVERN, 1969). The third term may be derived using the effective medium theory of BUDIANSKY and O'CONNELL (1976) for non-interacting cracks that dilate and contract in response to tension and compression (LYAKHOVSKY *et al.*, 1997b). The strain potential of damaged rock is further discussed in HAMIEL *et al.* (2011). Following LYAKHOVSKY *et al.* (1997a), we apply a damage model in which the elastic moduli are made to be simple functions of the damage state variable (α), and the evolution of damage is derived from 1, as follows:

$$\frac{\mathrm{d}\alpha}{\mathrm{d}t} = \begin{cases} C_{\mathrm{d}} I_2(\xi - \xi_0), & \text{for } \xi \geq \xi_0 \\ C_1 \exp\left(\frac{\alpha}{C_2}\right) I_2(\xi - \xi_0), & \text{for } \xi < \xi_0 \end{cases} \tag{2}$$

where $\xi = I_1/\sqrt{I_2}$ is referred to as the strain invariants ratio, and ξ_0 is a yielding threshold separating states of deformation involving material degradation ($\mathrm{d}\alpha/\mathrm{d}t > 0$ for $\xi > \xi_0$) and material healing ($\mathrm{d}\alpha/\mathrm{d}t < 0$ for $\xi < \xi_0$). Parameters C_{d}, C_1, C_2 are damage rate parameters constrained based on geophysical and experimental observations (LYAKHOVSKY *et al.*, 2001; FINZI *et al.*, 2011).

2.2. Time Integration Scheme for the Damage Rheology

In this section we outline an incremental formulation using the tangential tensor of the constitutive equations based on Eqs. 1 and 2. The scheme, which leads to a linear PDE to be solved in each loading step, can easily be implemented in the Escript PDE solver module (GROSS *et al.*, 2007). For more details on the implementation of incremental schemes in Escript we refer to GROSS *et al.* (2008).

By differentiating the strain potential (Eq. 1), the resulting stress can be written in a general "elastic" form (Eq. 3–5) using the effective elastic modules (λ_{eff}, μ_{eff}):

$$\sigma_{ij} = \lambda I_1 \delta_{ij} + 2\mu\varepsilon^{\mathrm{e}}_{ij} - \gamma\sqrt{I_2}\delta_{ij} - \gamma\frac{I_1}{\sqrt{I_2}}\varepsilon^{\mathrm{e}}_{ij} \tag{3}$$

$$\sigma_{ij} = \lambda_{\mathrm{eff}}\varepsilon^{\mathrm{e}}_{kk}\delta_{ij} + 2\mu_{\mathrm{eff}}\varepsilon^{\mathrm{e}}_{ij} \tag{4}$$

$$\lambda_{\mathrm{eff}} = \lambda - \gamma\frac{\sqrt{I_2}}{I_1}, \quad \mu_{\mathrm{eff}} = \mu - \gamma\frac{I_1}{2\sqrt{I_2}} \tag{5}$$

where ε^{e} and δ_{ij} stand for the elastic strain tensor and the Kronecker delta, respectively. In addition we adopt the LYAKHOVSKY *et al.* (1997a, b) formulation of elastic moduli and their dependence on damage (α), as follows:

$$\begin{aligned} \lambda &= \lambda_0 = \text{constant}; \\ \mu &= \mu_0 + \alpha\gamma_{\mathrm{m}}\xi_0; \\ \gamma &= \alpha\gamma_{\mathrm{m}}; \end{aligned} \tag{6}$$

where γ_{m} is the maximum value of the third elastic modulus defined by normalization of the damage variable (LYAKHOVSKY *et al.*, 1997a). The dependencies of elastic moduli on the damage variable produce the following changes during loading: as the damage variable α increases, the shear modulus μ decreases, Poisson ratio increases, and the modulus γ increases from 0 (damage free) to γ_{m} (LYAKHOVSKY *et al.*, 1997a).

Finally we consider the stress requirement in order to fulfill the momentum equation,

$$\sigma_{ij,j} = 0 \tag{7}$$

and we derive (based on Eq. 3–5) the tangential form the stress increment $\mathrm{d}\sigma_{ij}$ due to additional loading or deformation, as follows:

$$\begin{aligned} \mathrm{d}\sigma_{ij} &= \lambda_{\mathrm{eff}} d\varepsilon^{\mathrm{e}}_{kk}\delta_{ij} + 2\mu_{\mathrm{eff}} d\varepsilon^{\mathrm{e}}_{ij} + \frac{\partial\lambda_{\mathrm{eff}}}{\partial\varepsilon^{e}_{mn}}\mathrm{d}\varepsilon^{\mathrm{e}}_{mn}\varepsilon^{\mathrm{e}}_{kk}\delta_{ij} \\ &\quad + 2\frac{\partial\mu_{\mathrm{eff}}}{\partial\varepsilon^{e}_{mn}}\mathrm{d}\varepsilon^{\mathrm{e}}_{mn}\varepsilon^{\mathrm{e}}_{ij} + S_{ij}\,\mathrm{d}\alpha \\ S_{ij} &= \frac{\partial\lambda_{\mathrm{eff}}}{\partial\alpha}\varepsilon^{\mathrm{e}}_{kk}\delta_{ij} + 2\frac{\partial\mu_{\mathrm{eff}}}{\partial\alpha}\varepsilon^{\mathrm{e}}_{ij} \end{aligned} \tag{8}$$

with:

$$\begin{aligned} \frac{\partial\lambda_{\mathrm{eff}}}{\partial\varepsilon^{\mathrm{e}}_{mn}} &= -\gamma\frac{1}{I_1\sqrt{I_2}}\varepsilon^{\mathrm{e}}_{mn} + \gamma\frac{\sqrt{I_2}}{I_1^2}\delta_{mn} \\ \frac{\partial\mu_{\mathrm{eff}}}{\partial\varepsilon^{\mathrm{e}}_{mn}} &= -\frac{\gamma}{2}\frac{1}{\sqrt{I_2}}\delta_{mn} + \frac{\gamma}{2}\frac{I_1}{I_2^{3/2}}\varepsilon^{\mathrm{e}}_{mn} \\ \frac{\partial\lambda_{\mathrm{eff}}}{\partial\alpha} &= -\gamma_m\frac{\sqrt{I_2}}{I_1} \\ \frac{\partial\mu_{\mathrm{eff}}}{\partial\alpha} &= -\frac{\gamma_m}{2}\frac{I_1}{\sqrt{I_2}} \end{aligned} \tag{9}$$

and the term $S_{ij}\mathrm{d}\alpha$ (in Eq. 8) describing the stress increment due to damage evolution.

Equations 8 and 9 can be written in a more compact form using the fourth order tensor A^{e}_{ijmn}:

$$\begin{aligned}\mathrm{d}\sigma_{ij} &= A^{\mathrm{e}}_{ijmn}\,\mathrm{d}\varepsilon^{\mathrm{e}}_{mn} + S_{ij}\mathrm{d}\alpha \\ A^{\mathrm{e}}_{ijmn} &= \lambda_{\mathrm{eff}}\delta_{ij}\delta_{mn} + \mu_{\mathrm{eff}}(\delta_{im}\delta_{jn} + \delta_{in}\delta_{jm}) \\ &\quad + \gamma\frac{\sqrt{I_2}}{I_1}\left(\delta_{ij} - \frac{I_1}{I_2}\varepsilon^{\mathrm{e}}_{ij}\right)\left(\delta_{mn} - \frac{I_1}{I_2}\varepsilon^{\mathrm{e}}_{mn}\right)\end{aligned} \tag{10}$$

Viscous strain is introduced into the model by decomposing the total strain increment $\mathrm{d}\varepsilon_{mn}$ into an elastic part $\mathrm{d}\varepsilon^{\mathrm{e}}_{mn}$ and viscous strain part $\mathrm{d}\varepsilon^{\mathrm{v}}_{mn}$:

$$\mathrm{d}\varepsilon_{mn} = \frac{1}{2}\left(\mathrm{d}u_{m,n} + \mathrm{d}u_{m,n}\right) = d\varepsilon^{\mathrm{e}}_{mn} + \mathrm{d}\varepsilon^{v}_{mn} \tag{11}$$

where $\mathrm{d}u_m$ is the displacement increment. The viscous strain increment is given by

$$\begin{aligned}\mathrm{d}\varepsilon^{v}_{mn} &= \frac{\mathrm{d}t}{2\eta}\sigma'_{mn} \\ \frac{1}{\eta} &= \begin{cases} 2C_{\mathrm{v}}\frac{\mathrm{d}\alpha}{\mathrm{d}t} & \text{if } \frac{\mathrm{d}\alpha}{\mathrm{d}t} > 0 \\ 0 & \text{else} \end{cases}\end{aligned} \tag{12}$$

where C_{v} is a material parameter governing the rate of irreversible strain accumulation (Hamiel *et al.*, 2004a). The damage-related viscosity enables representation of the permanent inelastic deformation before brittle failure associated with micro-crack growth and frictional sliding between grains (Hamiel *et al.*, 2004a, b). Various studies have shown it is required to adequately describe processes such as subcritical crack growth and aseismic deformation in the seismogenic crust (Lyakhovsky and Ben-Zion, 2009; Ben-Zion and Lyakhovsky, 2006).

Combining Eqs. (10–12) leads to the following equation for the stress increment:

$$\mathrm{d}\sigma_{ij} = A^{\mathrm{e}}_{ijmn}(\mathrm{d}\varepsilon_{mn} - \mathrm{d}\varepsilon^{v}_{mn}) + S_{ij}\mathrm{d}\alpha \tag{13a}$$

where the damage increment $\mathrm{d}\alpha$ is derived from Eq. 2, as follows:

$$\mathrm{d}\alpha = \mathrm{d}t \cdot I_2(\xi - \xi_0) \cdot \begin{cases} C_{\mathrm{d}}, & \text{for } \xi \geq \xi_0 \\ C_1 \cdot \exp\left(\frac{\alpha}{C_2}\right) & \text{for } \xi < \xi_0 \end{cases} \tag{13b}$$

From the fact that the stress field needs to be divergence free (Eq. 7) we can establish the PDE for the displacement increment $\mathrm{d}u_m$:

$$-(A^{\mathrm{e}}_{ijmn}\mathrm{d}u_{m,n})_{,j} = \left(S_{ij}\mathrm{d}\alpha - A^{\mathrm{e}}_{ijmn}\frac{\mathrm{d}t}{2\eta}\sigma'_{mn}\right)_{,j} \tag{14}$$

which needs to be solved in each time step with suitable boundary conditions. With the calculated displacement increment $\mathrm{d}u_m$ we can update the elastic strain before entering the next time step:

$$\varepsilon^{\mathrm{e}}_{ij} \leftarrow \varepsilon^{\mathrm{e}}_{ij} + \mathrm{d}\varepsilon_{ij} - \frac{\mathrm{d}t}{2\eta}\sigma'_{ij} \tag{15}$$

The damage parameter is updated using a linearised backward Euler scheme (Eq. 13b).

2.3. Biaxial Compression Benchmark

In order to test our numerical formulation of the damage model we reconstruct the biaxial compression simulations and experimental results of Hamiel *et al.* (2004a) which are based on and compared to experimental results of Lockner *et al.* (1992). Two types of simulations are performed: a single-element simulation with homogeneous damage evolution under confined compression (biaxial test), and a multi-element simulation of heterogeneous damage evolution during biaxial compression tests with varying confining stress and strain rates. By comparing our numerical results to both a well established numerical code and laboratory experiments (Hamiel *et al.* 2004a and references within) we validate and benchmark our numerical procedure.

The biaxial simulation is setup with constant axial strain-rate and 50 MPa confining stress applied on a material corresponding to the experimental conditions and Westerly granite used by Hamiel *et al.* (2004a). The initial elastic moduli were evaluated based on the linear part of the stress–strain curves ($\lambda = 29$ GPa, $\mu_0 = 19$ GPa; see material GR1 in Hamiel *et al.*, 2004a). The damage related parameters were determined by Hamiel *et al.* (2004a) based on the onset of acoustic emissions (indicating $\xi_0 = -0.56$), the amount of irreversible strain and the overall shape of the stress–strain curve (best fitted using $C_{\mathrm{d}} = 3\ \mathrm{s}^{-1}$ and $C_{\mathrm{v}} = 2 \times 10^{-5}\ \mathrm{MPa}^{-1}$). The simulations were carried out as biaxial compression of a single-element domain (one element compressed until critical damage level is reached) and as multi-element domains of varying numeric resolution (using fine and coarse

meshes with number of elements ranging from 80×40 to 450×225, and domain size being 2×1 m). Our numeric simulations yielded stress–strain curves similar to both the numerical and experimental results described by HAMIEL *et al.* (2004a) (e.g., Fig. 1 single-element simulation with $C_v = 0$ simulation). The stress–strain curves indicate the different stages of deformation in compression tests, including initial elastic deformation, gradual distributed damage accumulation (with deviation from the linear elastic slope of the curve), the onset of damage localization (slope decreases and reaches peak stress) and finally macroscopic failure along a damaged shear-band. The post-failure stress-unloading path in the presented damage rheology is different than that expected from plasticity models (SCHREYER and CHEN, 1986), with steepness of stress–strain curve in the unloading regime not increasing in simulations with a multi-element domain.

3. Shear Band Analysis of the Damage Rheology Model

To better understand the deformation patterns resulting from our damage model we examine analytically the stability of a particular ground state with respect to perturbations in the form of shear bands (e.g., RUDNICKI and RICE, 1975). The class of ground states considered here are described by

$$\varepsilon_{22}^0 < 0, \quad \varepsilon_{11}^0 > 0, \quad \frac{\varepsilon_{11}^0}{\varepsilon_{22}^0} = -v \tag{16}$$

where v is the applied strain ratio (i.e., the negative of the ratio between lateral and axial deformation, at constant lateral stress). The strain-invariants ratio and effective elastic moduli can be rewritten as:

$$\xi = \frac{I_1^0}{\sqrt{I_2^0}} = -\frac{1-v}{\sqrt{1+v^2}}; \; \lambda_{\text{eff}}^0 = \lambda + \gamma \frac{\sqrt{1+v^2}}{1-v}, \quad \mu_{\text{eff}}^0 = \mu + \gamma \frac{1-v}{2\sqrt{1+v^2}} \tag{17}$$

The stress increments (Eq. 8) are rewritten in the following:

$$\begin{aligned} d\sigma_{11} &= A d\varepsilon_{11} + B d\varepsilon_{22} \\ d\sigma_{22} &= B d\varepsilon_{11} + C d\varepsilon_{22} \\ d\sigma_{12} &= 2\mu_{\text{eff}} d\varepsilon_{12} \end{aligned} \tag{18a}$$

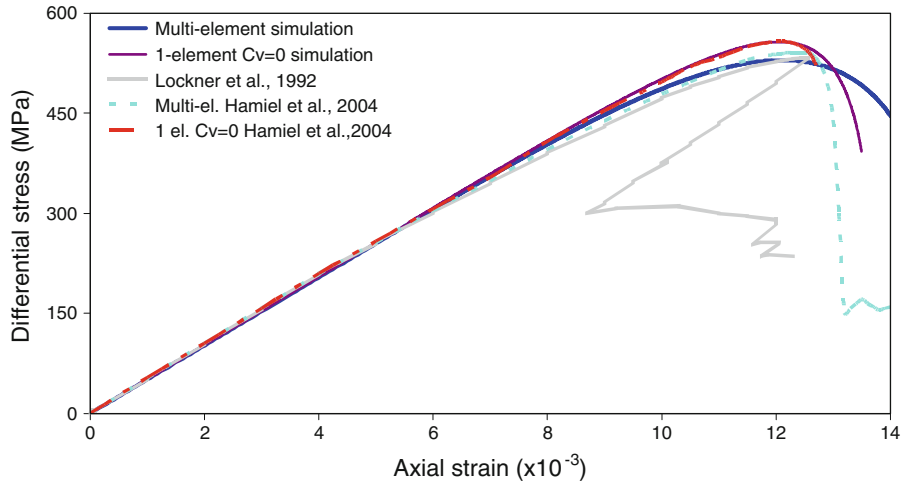

Figure 1

Stress–strain curves from our benchmark simulations shown to be comparable with Hamiel *et al.* (2004a) numerical results and Lockner *et al.* (1992) experimental results. The simulations with no damage-related inelastic deformation ($C_v = 0$) exhibit stress levels higher than those observed in the lab, and the multi-element simulations with $C_v = 2 \times 10^{-5}$ MPa^{-1} nicely reproduce the observations up to failure. Post-failure simulated curves are affected by the boundary conditions which do not enable unloading and reduction of the axial strain. In these simulations, domain size is 2×1 m and 1×1 m, and the number of elements is 150×75 and 1, for the multi- and single-element models, respectively

$$A = \lambda^0_{\text{eff}} + 2\mu^0_{\text{eff}} - \gamma\frac{\sqrt{1+v^2}}{1-v}\left(1+\frac{1-v}{1+v^2}v\right)^2$$
$$\text{where}: B = \left(\lambda^0_{\text{eff}} - \gamma\frac{\sqrt{1+v^2}}{1-v}\left(1+\frac{1-v}{1+v^2}v\right)\left(1-\frac{1-v}{1+v^2}\right)\right)$$
$$C = \left(\lambda^0_{\text{eff}} + 2\mu^0_{\text{eff}} - \gamma\frac{\sqrt{1+v^2}}{1-v}\left(1-\frac{1-v}{1+v^2}\right)^2\right) \tag{18b}$$

Insertion of (18a) into the plane strain stress equilibrium conditions yields:

$$A\mathrm{d}u_{1,11} + B\mathrm{d}u_{2,21} + \mu_{\text{eff}}\mathrm{d}u_{1,22} + \mu_{\text{eff}}\mathrm{d}u_{2,12} = 0$$
$$C\mathrm{d}u_{2,22} + B\mathrm{d}u_{1,12} + \mu_{\text{eff}}\mathrm{d}u_{1,21} + \mu_{\text{eff}}\mathrm{d}u_{2,11} = 0 \tag{19a}$$

Shear-band type solutions which are kinematically possible are obtained if the pde (Eq. 19a) is hyperbolic. These solutions are of the following form:

$$\begin{aligned}\mathrm{d}u_1 &= u(-x_1\sin\varphi + x_2\cos\varphi)\\ \mathrm{d}u_2 &= v(-x_1\sin\varphi + x_2\cos\varphi)\end{aligned}, \tag{19b}$$

where φ is defined as the angle between the less compressive principal strain axis and the shear-band. The equilibrium condition can be expressed as a single critical condition (Eq. 20) which is a function of the shear band angle (φ), the critical damage level (α) and the strain-ratio (v).

$$(A\sin^2\varphi + \mu_{\text{eff}}\cos^2\varphi)(C\cos^2\varphi + \mu_{\text{eff}}\sin^2\varphi) - (B+\mu_{\text{eff}})^2\cos^2\varphi\sin^2\varphi = 0 \tag{20}$$

The shear band characteristics (φ, α, v) naturally emerging from our damage model are determined by numerical analysis of this critical condition and determination of the parameters corresponding to the lowest critical damage level for a range of strain-ratio settings. In other words, in Eq. 20 we fix the strain-ratio ($0 < v < 1.6$) and find all real solutions with damage levels lower than 1. As the shear band with the lowest damage level is the one expected to form first (in a compressed material with accumulating damage), we can determine the shear band angle (and damage level) expected in any compression test based on the boundary strain-ratio settings. Our analysis shows that damage values in a narrow range around the lowest damage level correspond to large variations of the shear band angle (up to $\pm 3°$). This is portrayed in Fig. 2 as the wide scatters of calculated shear band angles (open blue diamonds) corresponding to narrow scatters of calculated damage

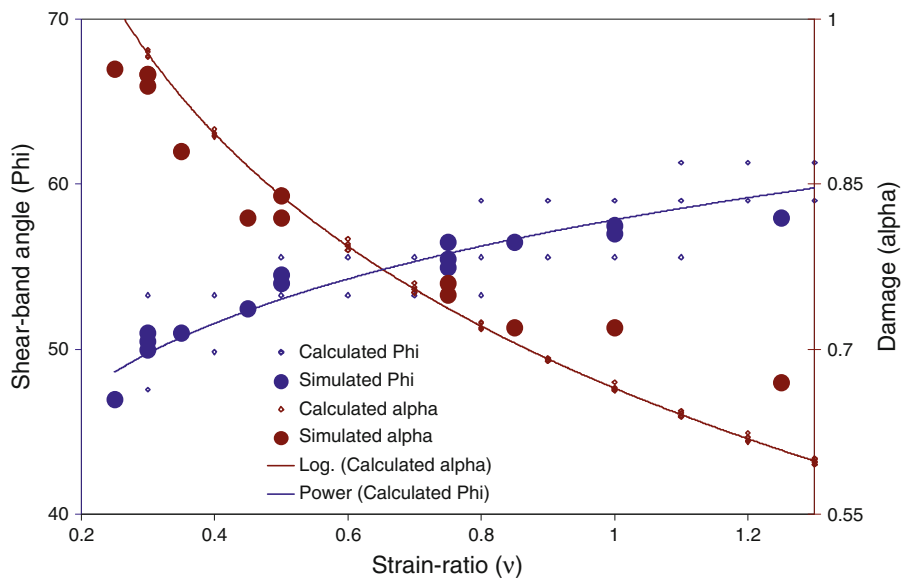

Figure 2

Analytically derived and numerical observations of shear-band characteristics. Shear band angle (φ) and critical damage level (α) calculated using Eqs. 16–20 (*scattered*, *open diamond data-points* and *regression-lines*) compared with numerical results in simulations with strain-ratio (v) between 0.2 and 1.3 (*filled blue* and *red circle symbols*, for φ and α respectively). Regression lines for the analytically derived values were added to enhance the illustration. The *scatter* in simulated values of damage (α) is predominantly attributed to measuring inaccuracy (see text)

levels (open red diamonds). For instance, in a compression test with $v = 0.8$, the three most plausible solutions satisfying the critical condition with the lowest damage levels correspond to critical damage levels of $\alpha = 0.72 \pm 0.01$ and shear band angles of $\varphi = 53$–$59°$. Figure 2 compares the calculated shear band angles and critical damage levels with observations of these characteristics in biaxial compression simulations with a range of strain-ratios (strain rate boundary condition, 2×1 m domain with 250×125 elements).

We note that determination of the simulated shear band angle is not of very high accuracy (estimated error $\pm 2°$), particularly as we wish to determine the angle during the early stages of shear band formation (before it widens and extends towards the domain boundaries). Nevertheless, as the shear band angle is consistent in simulation with increased element density and the analytically derived shear band angles have a similar (and typically larger) range of variability, we consider the accuracy of simulated angles as sufficient. In addition, we wish to focus the attention on the trend of decreasing shear band angles in compression tests with decreasing strain-ratio. Both the numeric simulations and the shear band analysis suggest a shear band angle of $\sim 60°$ in compression tests with high strain-ratios ($v = 1.3$–1.5), and much lower shear band angles (45–50°) in compression tests with low strain-ratios ($v = 0.25$–0.35). Our results indicating shear bands close to 45° in highly confined compression tests and inclinations steeper by 10–15° in tests with transverse tensional stress ($v > 1$) conform with experimental observations (e.g., Bardet, 1991; Besuelle, 2001) and with numerical and theoretic results (e.g., Rudnicki and Olsson, 1998; Rudnicki, 2002). In particular, our shear band orientations ($45° < \varphi < 60°$) and the decrease in angle with increase of confinement correspond closely to analytic predictions for a rock with Poisson's ratio of approximately 0.25 and a sum of dilation and friction parameters (β, μ, respectively) approximately equal to 0.8 (Rudnicki and Olsson, 1998; their Eqs. 10–15).

The comparison to theoretical predictions based on plasticity and to experimental observations is limited however. The classic shear band analysis, identifying instabilities in the homogeneous solution, is sensitive to the applied constitutive relations (Rudnicki and Rice, 1975; Rudnicki, 2002) and it describes band orientation as a function of parameters such as friction and dilatancy angles which are not readily determined in our simulations (as we apply a damage rheology rather than a friction law). The experimental results are typically characterized by a large scatter in band orientation (Olsson, 1999; Desrues and Chambon, 2002) and large deviations from the orientations estimated based on friction and dilatancy angles observed at the time of failure (these calculations overestimate orientations by 10–36 % according to Bardet, 1991). In addition, the experimental results are obtained in experiments with fixed confining stress (without rigorous documentation of strain ratio which is used as boundary condition in our simulations), and they exhibit a significant spatio-temporal variation in friction and dilatancy angles which have been shown theoretically to significantly effect shear band orientation (Bardet, 1991; Rudnicki and Olsson 1998). Nevertheless, the theoretic predictions and laboratory observations of shear bands in rocks equivalent to those represented in our simulations (i.e., Poisson's Ratio ~ 0.25; Initial internal friction ~ 0.6; Low porosity rock) indicate that shear-band orientations range from about 40–50° in highly confined experiments to about 55–65° in experiments with low confinement, which is in good agreement with our results.

The main discrepancy between our analytic predictions and our numerical results was in the critical damage levels in compression tests with high strain ratios (where significant transverse tensional strain is applied). While our analysis predicts that shear bands should form at damage levels of $\alpha < 0.65$ (for $v > 1.0$), the simulations exhibit strain localization at significantly higher damage levels (with discrepancies $\Delta\alpha = 0.05$–0.12, increasing with increasing v). The discrepancy may be viewed as an indication that the shear band analysis with the chosen ground-state does not apply for the tensional regime prevailing in compression tests with such high strain-ratio (i.e., where transverse extension is as great or greater than axial compression). Alternatively, the high damage levels observed along simulated shear bands may be a result of not incorporating a strain-ratio dependent

critical damage value as suggested by LYAKHOVSKY *et al.* (1997a, b). The critical damage level is equivalent to a yield criterion derived from the condition for convexity loss (which is used in the model to derive the value of γ_{max}). According to the instability analysis of LYAKHOVSKY *et al.* (1997a, b), failure is expected to occur at $\alpha = 1$ in highly confined compression (where the strain invariants ratio at the site of strain localisation is approximately $\xi = \xi_0$) and at much lower values ($\alpha \approx 0.7$) in extension (i.e., where $\xi = +0.5$). Implementing a variable critical damage level in our numerical code would lower the damage level at which shear bands are formed (especially at high strain ratios), and it would reduce the discrepancy between predicted and simulated critical damage values.

Finally we note that shear-band orientation in our simulations shows no mesh dependency within the range of meshes used (between 80 × 40 elements to 450 × 225 elements in a domain of 2 × 1 m). Nevertheless, as expected in such numerical study, the width of shear zone is mesh-dependent (MUHLHAUS and VARDOULAKIS, 1987). Simulated shear band width in the current work is typically 1–3 elements wide (but wider at the nucleation site which is also the intersection of two bands). For the above reasons we compare numerical, experimental and analytical orientations of shear-bands rather than focus on shear band width.

4. Discussion

The application of damage rheology in simulations of crustal deformation may yield many insights in the study of evolving fault-structures and strain-localization processes. Using the model described in this paper we examined some of the characteristics of evolving shear-bands in simulations of compression tests. We describe here the stages of progressive deformation and strain-localization in terms of evolving damage levels and volumetric strain observed in the shear bands. We discuss our findings in the context of recent observations and theoretical studies focused on compaction and dilation bands (e.g., RUDNICKI, 2002; AYDIN *et al.*, 2006; HOLOCOMB *et al.* 2007; ISSEN 2008).

4.1. Localized Dilation Within Shear-Bands in Compression Tests

We find that within a wide range of strain ratios ($v = 0.25$–1.6), the shear bands exhibit local dilation ($I_1 > 0$). In addition, such simulated shear bands exhibit a transition from positive to negative values of the effective elastic modulus λ_{eff} (i.e., the effective value of the first Lame parameter; see Eq. 5). However, in simulations with a very low strain ratio ($v < 0.25$; representing highly confined compression) localization and dilation do not occur. The latter result is also predicted by our shear-band analysis in which the critical condition for kinematically plausible solutions (Eqs. 16–20) could not be satisfied for $v < 0.2$. Homogeneous compression and weak localization (or lack of it) in compression tests with high confining stress (i.e., >200 MPa and/or $v \approx 0.2$ and therefore $\xi \approx \xi_0$) are in agreement with experimental results (e.g., WONG *et al.*, 1997; WU, 2000; MENENDEZ, 1996), with recent studies of compaction bands and compacting shear bands (CHALLA and ISSEN, 2004; ISSEN 2008) and with theoretical and numerical analysis of a coupled damage-porosity model (HAMIEL *et al.*, 2004b, 2005). The conditions in which strain is not localized along shear-bands could represent a transition from brittle failure to distributed cataclastic flow in which compaction, pore collapse, strain-hardening and intensive grain crushing is dominant (WU 2000; MENENDEZ 1996). Alternatively, ISSEN (2008) suggest the formation of a localized compaction band could represent conditions in which the intermediate principal stress is equal to the minimum compressive stress. The scarcity of compaction-band observation (AYDIN *et al.*, 2006. HOLOCOMB *et al.*, 2007) could then be viewed as indication that these conditions are transient, allowing the thickening of bands with ongoing loading and strain (ISSEN, 2008).

In simulations with moderate or relatively high confining stress (i.e., low strain-ratio), dilation is observed only after the shear band forms and starts propagating, and primarily near the nucleation site of the shear bands where conjugate bands intersect and a wide region of fully damaged material forms. This observation suggests that dilation is not a necessary condition for damage and strain localization and for

shear band formation. Alternatively, it could indicate that for non-porous rocks at relatively high confining pressure, pre-failure volumetric changes are small and highly depend on the stress state. Experimental and theoretic work with rocks of a large range of porosity indicate that while pre-failure damage is mostly intergranular cracking with limited or no dilatancy (depending on initial porosity and confinement), post-localization damage within the shear band is extensive and is associated with dilatancy and enhanced tensile stress at grain contacts (Menendez, 1996; Wu, 2000). Finally, some studies suggest that at moderate to high confining pressure, shear-induced dilation and inelastic compaction processes (e.g., distributed grain crushing and pore collapse) could coexist and interact to form compacting shear band and conjugate pure shear bands (Challa and Issen, 2004), or deformation in distinct domains of either dilating shear bands or arrays of compaction bands (Baud *et al.*, 2004). In any case, where dilation occurs it introduces a positive feedback effect in which it enhances damage accumulation and material weakening which in turn results in further strain-localization and deformation (dilation and shear).

The progressive evolution of damage and local dilation associated with shear bands in our simulations can be described by the following stages: The initial stage of deformation (Fig. 3 left) consists of homogeneous compression and defuse, gradual damage-accumulation (in simulation with high confining stress this could be preceded by partial healing of initial damage in the prescribed nucleation site). The following stage consists of strain-localization, local damage accumulation and local reduction in compression around the nucleation site (Fig. 3, second panel). The formation of conjugate shear bands follows with a transition from compaction to dilation at the nucleation site (where the shear bands intersect; Fig. 3 third panel). Propagation of the dilating shear band is characteristic of the fourth stage (Fig. 3, right panel). As mentioned above, dilation does not necessarily occur within the entire shear band, and typically the tips of the propagating bands experience pure-shear or even slight compression. Finally, widening of the shear-bands and diffusion of the strain may occur with persisting dilation or a transition to defuse compression, depending on the boundary conditions driving the deformation. The emerging progression in simulated shear bands is in agreement with theoretical predictions and experimental results (Hamiel *et al.*, 2005; Lyakhovsky and Hamiel, 2007; Besuelle, 2001; Wu, 2000; Issen, 2008).

The progression of deformation also involves the evolution of elastic moduli and strain-potential within the shear bands. As expected from the constitutive

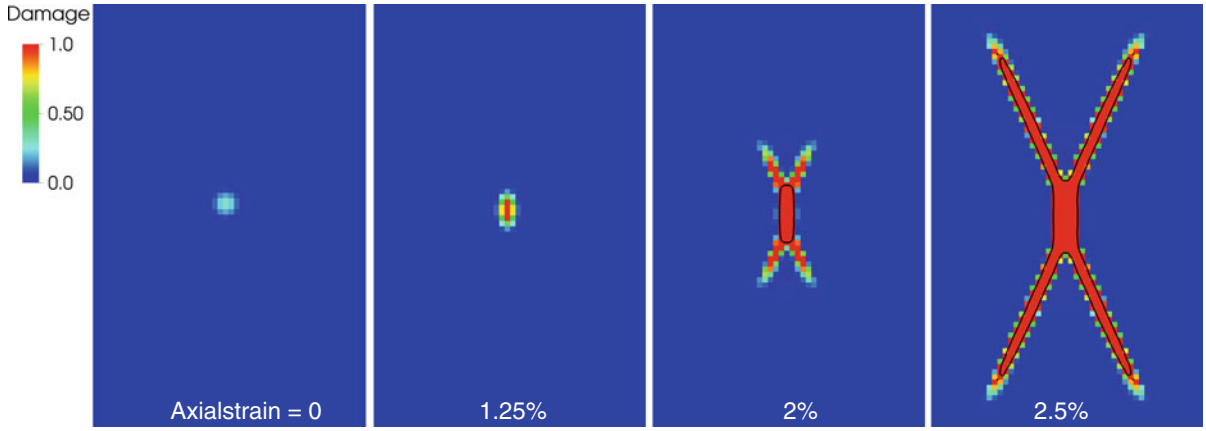

Figure 3

Shear band characteristics observed in simulations of confined bi-axial compression tests ($\nu = 0.35$). The snapshots show the damage level (α) and dilating zone (*black line* outlining zone with positive volumetric-strain, $I_1 > 0$) during progressive compression (at axial strains of 0, 1.25, 2 and 2.5 %). The snapshots represent the transition from homogeneous compression and subtle healing of initial damage in the prescribed nucleation site (*left*), through damage accumulation (strain = 1.25 %), formation of shear bands and transition from compaction to dilation, propagation and eventually widening of the dilating shear band (*right*). We note that I_1 is a measure of volume change, and therefore, some limited band-perpendicular dilation may occur at $I_1 < 0$ where band-parallel compression prevails

model, damage accumulation is associated with degradation of material rigidity (Eq. 6) and with degradation of the effective elastic moduli (Eq. 5). However, while μ_{eff} decreases monotonously with increasing damage and strain-invariants ratio (ξ), λ_{eff} has a singular point at $\xi = 0$, which results in a transient phase of negative λ_{eff} values and enhances strain localization and dilation within the shear-band. Simulations with highly confined conditions ($\nu < 0.3$) exhibit rather homogeneous compaction until the above singularity point is approached (locally in one element or a cluster of model elements) followed by the emergence of a shear band. Finally, as damage accumulates and the strain-invariants ratio becomes significantly high, the strain-potential of material in shear-bands decreases significantly ($U < 0.5U_0$ for $\alpha = 1$, $\xi \sim -0.1$; and $U < 0.25U_0$ for $\alpha = 1$, $\xi \sim +0.1$).

4.2. *Applicability of the Analysed Damage Model for Studies of Crustal Deformation*

The analysed damage model has been applied successfully in numerous studies of crustal deformation (e.g., Lyakhovsky *et al.*, 2001; Ben-Zion and Lyakhovsky, 2006; Finzi *et al.*, 2009). In the numerical framework by Lyakhovsky and Ben-Zion, co-seismic localization is enhanced by introducing a co-seismic plastic strain (equivalent to Drucker–Prager plasticity calculated for fault-slip), an abrupt stress redistribution procedure in which the shear stress is reduced to a residual level in elements that reached a critical damage level, and a dynamic weakening procedure involving a co-seismic reduction of the critical damage level (Lyakhovsky *et al.*, 2001; Ben-Zion and Lyakhovsky, 2006; Lyakhovsky and Ben-Zion, 2008). Following our analysis of the damage rheology we believe that the constitutive model itself (without a yield criterion and additional co-seismic procedures) is a sufficient mechanism for strain-localisation and is adequate for simulating shear-band formation in the brittle upper-crust. Various modifications could be considered to better represent natural deformation in the brittle crust using this damage rheology model:

1. The degradation of material strength should be tapered and the strength should reach a minimal level after which additional damage would not have significant further effect. Introduction of such a criterion into the model could be done by simply using a non-linear function for the damage-related modulus and it's dependence on the damage-state variable (i.e., $\gamma = \gamma_{\max} \cdot \exp(1 - n\alpha)$). Using such a form for the damage-related modulus would taper the effect of additional damage to an already extensively damaged material, and it will eliminate the need to define a critical damage level and a transition to plasticity. However, calibration of the additional parameters in the equation for the damage-related modulus would require information on post-failure characteristics of rocks, which are difficult to measure. Preliminary simulations with such a modified model yielded reasonable results with stress–strain curves comparable to experimental results. However, in these experiments homogeneous damage accumulation, after the shear-bands are fully formed, delocalises the strain distribution yielding a fully damaged domain with significantly reduced effective elastic moduli (Fig. 4). In this simulation we use $\gamma = \gamma_{\max} \cdot \exp(1 - n\alpha)$ with $n = 1.25$ which results in relatively low values of $\gamma_{\max}$ (for $\alpha = 1$) and relatively high residual effective rigidity ($\sim$30 %) and strain-potential ($\sim$20 %; Fig. 4).

An alternative approach could consist of a criterion for minimum effective rigidity and/or minimum strain energy beyond which further damage accumulation would have little or no additional effect on the material properties. This kind of criteria could obviously prevent unrealistic situations in which simulated material display negative effective rigidity or negative strain potential. Derivation of such criteria could complement and strengthen the Lyakhovsky and Ben-Zion criterion for instability which is based on a strain energy convexity-loss condition (Lyakhovsky and Ben-Zion, 2008).

2. As in the theory of plasticity, the model formulation needs to incorporate a local unloading criterion. Such a criterion indicates the transition from dissipative to non-dissipative deformation. Such a criterion is necessary for the representation of sharp shear bands in the context of strain softening type behaviour to consider unloading outside zones of localized strain. The present formulation of the damage model does not contain a strain rate sensitive

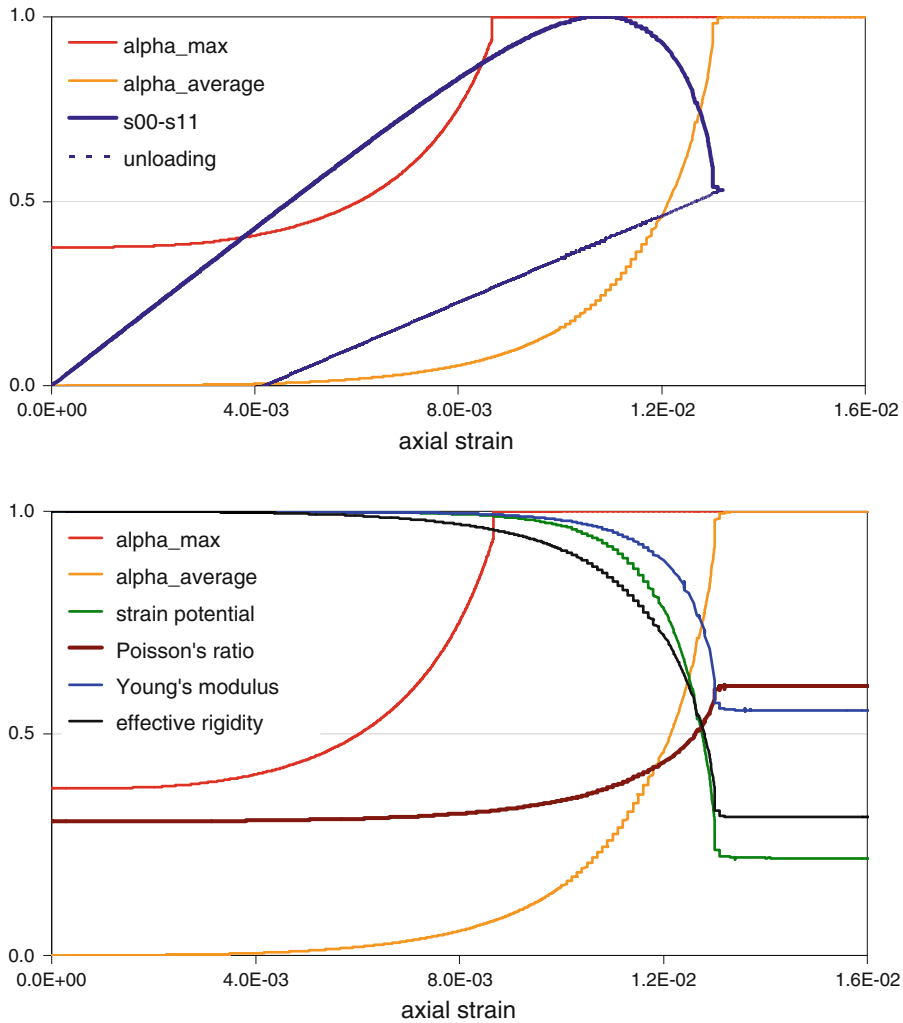

Figure 4

Normalised stress–strain curve (*top panel*) superimposed with damage levels within the shear band (*red line*) and overall average damage (*orange line*), average values of the elastic moduli and strain-potential (normalised, *bottom panel*), and average value of the Poisson's ratio (actual value, *brown line*, *bottom panel*). The stress unloading path (*dashed blue line*, *top panel*) is calculated based on the residual effective Young's modulus. This simulation consisted of a compression test with no confining stress, a non-linear expression for γ (see text), and otherwise similar parameters as previous simulations

unloading criterion. In the absent of such unloading criterion, the co-seismic localization and quasi-dynamic propagation processes applied by Lyakhovsky and co-authors are necessary for simulations of multi earthquake crustal deformation.

3. Finally, the tangential formulation of the damage model consists of a singular point where $\xi = 0$ (and λ_{eff} is unbound), and it yields negative effective elastic moduli (the transient phase of $\lambda_{\text{eff}} < 0$ mentioned above, and eventually with $\alpha = 1$ and $\xi \gg 0$ also $\mu_{\text{eff}} < 0$) and negative strain-potential (also for $\alpha = 1$ and $\xi \gg 0$). These shortfalls indicate that a more stable numerical formulation is required in order to apply the damage rheology model in simulations of long term crustal deformation.

References

Allix, O. and Hild, F. (2002), Continuum Damage Mechanics of Materials and Structures, Elsevier, p. 396. Amsterdam Holland.

Alm, O., Jaktlund, L.L., and Kou, S. (1985), *The influence of microcrack density on the elastic and fracture mechanical*

properties of Stripa granite, Phys. Earth Planet. Inter., *40*, 161–179.

Aydin, A., Borja, R., Eichhubl, P. (2006), *Geological and mathematical framework for failure modes in granular rock*. J Struct. Geol *28*:83–93.

Bardet J. P. (1991), *Orientation of shear bands in frictional soils*. J. Eng. Mech. *117*:1466–1484.

Baud, P., Klein, E., Wong, T-F., (2004), *Compaction localization in porous sandstones: spatial evolution of damage and acoustic emission activity*. J Struct Geol *26*:603–624.

Ben-Zion, Y. and Sammis, C. (2003), *Characterization of Fault Zones*, Pure Appl. Geophys. *160*, 677–715.

Ben-Zion, Y. and Lyakhovsky, V. (2006), *Analysis of aftershocks in a lithospheric model with seismogenic zone governed by damage rheology*, Geophys. J. Int. *165*, 197–210.

Ben-Zion, Y. (2008), *Collective Behavior of Earthquakes and Faults: Continuum-Discrete Transitions, Progressive Evolutionary Changes and Different Dynamic Regimes*, Rev. Geophysics, *46*, RG4006, doi:10.1029/2008RG000260, 2008.

Besuelle, P. (2001), *Compacting and Dilating Shear Bands in Porous Rock: Theoretical and Experimental Conditions*, J. Geophys. Res. *106*, 13435–13442.

Biot, M.A. (1965), The mechanics of incremental deformations, Wiley, New York.

Buck, W.R. (1991), *Models of Continental Lithosphere Extension*, J. Geophys. Res, *96*(B12), 20161–20178.

Budiansky, B. and O'Connell, R. J. (1976), *Elastic moduli of a cracked solid*, Int. J. Sol. Struct. *12*, 81–97.

Challa and Issen, (2004), *Conditions for compaction band formation in porous rock using a two yield surface model*, Journal of Engineering Mechanics *130* (2004), pp. 1089–1097.

Chen, W.F. (1975), Limit analysis and soil plasticity, Elsevier, Amsterdam.

Chester, F. M., and Logan, J.M. (1986), *Implications for mechanical properties of brittle faults from observations of the Punchbowl fault zone, California*. Pure Appl. Geophys. *124*, 79–106.

Chester, F. M., Evans, J. P., and Biegel, R. L. (1993), *Internal structure and weakening mechanisms of the San Andreas Fault*, J. Geophys. Res. *98*, 771–786.

Desrues, J., Chambon, R., (2002), *Shear band analysis and shear moduli calibration*, International Journal of Solids and Structures *39*, 3757–3776.

England, P. (1983), *Constraints on Extension of Continental Lithosphere*, J. Geophys. Res., *88*(B2), 1145–1152.

Evans, J. P., Shipton, Z. K., Pachell, M. A., Lim, S. J., and Robeson, K. (2000), The structure and composition of exhumed faults, and their implication for seismic processes. In Proc. of the 3rd Confer. on Tecto. problems of the San Andreas system, (Stanford University 2000).

Finzi, Y., Hearn, E.H., Ben-Zion, Y., and Lyakhovsky, V. (2009), *Structural properties and deformation patterns of evolving strike-slip faults: Numerical simulations incorporating damage rheology*. Pure and Appl. Geophys., vol. *166*, N. 10, 2009.

Finzi, Y., Hearn, E. H., Lyakhovsky, V., and Gross, L. (2011), *Fault-zone healing effectiveness and the structural evolution of strike-slip fault systems*, Geophys. J. Int., *186*, 963–970.

Gibbs, A.D. (1984), *Structural evolution of extensional basin margins*, J. Geo. Society *141*, pp. 609–620.

Gross, L., Bourgouin, L., Hale, A. J., and Muhlhaus, H. (2007), *Interface modelling in incompressible media using level sets in Escript*, Physics of the Earth and Planetary Interiors, *163*, 23–34, doi:10.1016/j.pepi.2007.04.004.

Gross, L., Muhlhaus, H., Thorne, E., and Steube, K. (2008), *A new design of scientific software using Python and XML*, Pure Appl. Geophys., *165*, 653–670, doi:10.1007/s00024-008-0327-7.

Hamiel, Y., Liu, Y., Lyakhovsky, V., Ben-Zion, Y., and Lockner, D. (2004a), *A visco-elastic damage model with applications to stable and unstable fracturing*, Geophys. J. Int. *159*, 1155–1165.

Hamiel, Y., Lyakhovsky, V., and Agnon, A. (2004b), *Coupled evolution of damage and porosity in poroelastic maedia: theory and applications to deformation of porous rocks*, Geophys. J. Int. *156*, 701–713.

Hamiel, Y., Lyakhovsky, V., and Agnon, A. (2005), *Poroelastic damage rheology: Dilation, compaction, and failure of rocks*. Geochem. Geophys. Geosyst., *6*, Q01008, doi:10.1029/2004GC000813.

Hamiel, Y., Lyakhovsky, V., Ben-Zion, Y. (2011), *The elastic strain energy of damaged solids with applications to nonlinear deformation of crystalline rocks*. Pure Appl. Geophys., doi:10.1007/s00024-011-0265-7.

Hill, R. and Hutchinson, J.W. (1975), *Bifurcation phenomena in the plane strain tension test*, J. Mech. Phys. Solids *23*, pp. 239–264.

Hill, R. (1998), The Mathematical Theory of Plasticity, Oxford University Press, Oxford.

Hobbs, B. E., Muhlhaus, H.-B., Ord, A. (1990), Instability, softening and localization of deformation. In: A.Deformation mechanisms, rheology and tectonics. Editors: Knipe R.J., Rutter E.H., Geol. Soc., London; Special Publication, *54*, 143–165.

Holocomb D., J.W. Rudnicki, K.A. Issen, K. Sternlof, (2007), *Compaction localization in the Earth and the laboratory: state of the research and research directions*, Acta Geotechnica (2007) *2*:1–15, doi:10.1007/s11440-007-0027-y.

Issen, K. A., and V. Challa, (2008), *Influence of the intermediate principal stress on the strain localization mode in porous sandstone*, J. Geophys. Res., *113*, B02103, doi:10.1029/2005JB004008.

Kim, Y. S., Peacock, D. C. P., and Sanderson, D. J. (2004), *Fault damage zones*, J. Struct. Geology *26*, 503–517.

Lemiale, V., Muhlhaus, H.-B., Moresi, L., Stafford, J. (2008), *Shear banding analysis of plastic models formulated for incompressible viscous flows*. Physics of the Earth and Planetary Interiors Volume *171*, Issue 1–4, 177–186.

Lockner, D.A., Byerlee, J.D., Kuksenko, V., Ponomarev, A., and Sidorin, A., (1992), Observations of quasi-static fault growth from acoustic emissions, in Fault Mechanics and Transport Properties of Rocks, International Geophysics Series, Vol. *51*, 3–31, eds. Evans, B. & Wong, T.-F., Academic Press, San Diego, CA.

Lubliner, J. (1990), Plasticity Theory, Macmillan Publishing, New York.

Lyakhovsky, V. and Myasnikov, V. P. (1984), *On the behavior of elastic cracked solid*, Phys. Solid Earth *10*, 71–75.

Lyakhovsky, V. and Myasnikov, V. P. (1985), *On the behavior of visco-elastic cracked solid*, Phys. Solid Earth *4*, 28–35.

Lyakhovsky, V., Ben-Zion, Y., and Agnon, A. (1997a), *Distributed damage, faulting, and friction*, J. Geophys. Res. *102*, 27,635–27,649.

Lyakhovsky, V., Reches, Z., Weinberger, R., and Scott, T.E. (1997b), *Non-linear elastic behavior of damaged rocks*, Geophys. J. Int. *130*, 157–166.

Lyakhovsky, V., Ben-Zion, Y., and Agnon, A. (2001), *Earthquake cycle, faults, and seismicity patterns in rheologically layered lithosphere*, J. Geophys. Res. *106*, 4103–4120.

LYAKHOVSKY, V. and HAMIEL, Y. (2007), *Damage evolution and fluid flow in poroelastic rock. Izvestiya*, Physics of the Solid Earth, *43*: 13–23.

LYAKHOVSKY, V. and BEN-ZION, Y. (2008), *Scaling relations of earthquakes and aseismic deformation in a damage rheology model*, Geophys. J. Int. *172*, 651–662, doi:10.1111/j.1365-246X.2007.03652.x.

LYAKHOVSKY, V. and BEN-ZION, Y. (2009), *Evolving geometrical and material properties of fault zones in a damage rheology model*, Geochem. Geophys. Geosyst., *10*, Q11011, doi:10.1029/2009GC002543.

MALVERN, L.E. (1969), Introduction to the Mechanics of a Continuum Medium (New Jersey, Prentice-Hall, Inc., 1969), 713 pp.

MENENDEZ, B., W. ZHU and T.F. WONG, 1996, *Micromechanics of brittle faulting and cataclastic flow in Berea sandstone*, Journal of Structural Geology *18*, 1–16.

MITCHELL T. and D. FAULKNER, (2009), *The nature and origin of off-fault damage surrounding strike-slip fault zones with a wide range of displacements: A field study from the Atacama fault system, northern Chile*, Journal of Structural Geology *31*, 802–816, doi:10.1016/j.jsg.2009.05.002.

MORESI, L. and MUHLHAUS, H.B. (2006), *Anisotropic viscous models of large-deformation Mohr-Coulomb failure*, Phill. Magazine *86*, pp.3287–3305.

MUHLHAUS, H.-B., VARDOULAKIS, I. (1987), *Thickness of shear bands in granular materials*, Geotechnique. Volume *37*, Issue 3, September 1987, Pages 271–283.

OLSSON, W.A., 1999. *Theoretical and experimental investigation of compaction bands*. Journal of Geophysical Research *104*, 7219–7228.

RICE, J.R., (1983), *Constitutive relations for fault slip and earthquake instabilities*. Pure Appl. Geophys. *121*, 443–475.

ROCKWELL, T. K. and BEN-ZION, Y. (2007), *High localization of primary slip zones in large earthquakes from paleoseismic trenches: Observations and implications for earthquake physics*, J. Geophys. Res. *112*, B10304, doi:10.1029/2006JB004764.

RUDNICKI, J. W., and RICE, J. R. (1975), *Conditions for the localization of deformation in pressure-sensitive dilatant materials*, J. Mech. Phys. Solids, *23*, 371–394.

RUDNICKI, J. W., and OLSSON, W. A. (1998), *Re-examination of fault angles predicted by shear localization theory*, Int. J. Rock Mech. Min. Sci., *35*, 4–5.

RUDNICKI R.W., (2002), *Conditions for compaction and shear bands in a transversely isotropic material*. International Journal of Solids and Structures *39*, 3741–3756.

SCHULTZ R.A., R. SOLIVA, H. FOSSEN, C.H. OKUBO and D.M. REEVES, (2008), *Dependence of displacement–length scaling relations for fractures and deformation bands on the volumetric changes across them*, Journal of Structural Geology *30*, pp. 1405–1411.

SCHULZ, S. E. and EVANS, J. P. (2000), *Mesoscopic structure of the Punchbowl Fault, Southern California and the geologic and geophysical structure of active strike-slip faults*, J. of Struct. Geol. *22*, 913–930.

SCHREYER H. L. and CHEN Z. (1986), *One-dimensional softening with localization*, J. Appl. Mech. *53*, 791 (1986), doi:10.1115/1.3171860.

SIBSON, R. H. (2003), *Thickness of the seismic slip zone*, Bull. Seismol. Soc. Am. *93*, 3, 1169–1178.

TURCOTTE, D. L. and GLASSCOE, M.T. (2004), *A damage model for the continuum rheology of the upper continental crust*, Tectonophysics *383*, 71–80.

TVERGAARD, V., NEEDLEMAN, A. and Lo, K.K. (1981), *Flow localization in the plane strain tensile test*, J. Mech. Phys. Solids *29*, pp. 115–142.

WALSH, J., WATTERSOV, J. and YIELDING, G. (1991), *The importance of small-scale faulting in regional extension*, Nature *351*, pp. 391–393.

WATTS, A.B., BONDIE, J.H. and STECKLER, M.S. (1980), *Observation of flexure and the state of stress in the oceanic lithosphere*, J. Geophys. Res. *85*, pp. 6369–6376.

WONG, T., DAVID, C. and ZHU, W. (1997), *The transition from brittle faulting to cataclastic flow in porous sandstones: Mechanical deformation*, J. Geophys. Res., *102*, 3009–3025.

WU, X. Y., P. BAUD and T. F. WONG, (2000), *Micromechanics of compressive failure and spatial evolution of anisotropic damage in Darley Dale sandstone*, International Journal of Rock Mechanics and Mining Sciences *37*, pp. 143–160.

(Received February 28, 2011, revised January 16, 2012, accepted January 25, 2012)